Scanning electron microscopy[☆]

Anjam Khursheed, Department of Electrical and Computer Engineering, National University of Singapore, Singapore, Singapore

© 2022 Elsevier Ltd. All rights reserved.

Introduction	1
SEM basic principles	1
Electron optical figures of merit	5
Summary and future directions	14
Acknowledgments	14
Conflict of Interest	14
References	14

Introduction

The scanning electron microscope (SEM) is an indispensable research and development tool in the subject of condensed matter physics. It is the most widely used instrument for examining the surface topography and morphology of bulk materials on the nanoscale. It is capable of routinely obtaining an image resolution of 1–2 nm on a variety of different materials, a factor of around 200 times better than the spatial resolution of conventional optical microscopes.

In the category of electron microscopes, the SEM is smaller, cheaper, and more accessible than a transmission electron microscope (TEM) or a scanning transmission electron microscope (STEM). Its specimens require much less preparation and its images are much easier to interpret. These advantages come from the fact that it functions by detecting reflected/scattered electrons from bulk specimens rather than relying on an electron beam propagating through a thin specimen (nm thick), as is the case with transmission electron microscopes. These advantages come at the price of its overall image resolution being around an order of magnitude poorer than those that can be obtained by a TEM or a STEM. In general, however, the SEM plays a complementary role to transmission electron microscopes. It provides information on a sample's surface and its composition, while a TEM or STEM acquires information on the inner structure of the sample, such as crystal structure.

Several companion analytical tools have been developed for the SEM that transform it into a powerful material analysis tool, taking it beyond a purely topographical imaging mode of operation. The energy dispersive X-ray (EDX) spectroscopy technique for instance, is used in the SEM to capture atomic transitions that emit characteristic X-rays, enabling it to carry out quantitative material analysis. The electron backscatter diffraction technique (EBSD) inside the SEM is routinely used to provide a material's crystal structure, orientation, phase, and strain information. SEMs have also been developed to operate with a gaseous environment inside the specimen chamber, which provides the option of using wet samples and uncoated non-metallic samples. These SEMs are known as environmental SEMs (ESEMs). There have also been many other advances, such as the inclusion of a gun monochromator unit to lower the primary beam energy spread, further improving the electron optics of SEMs. However, the focus of this chapter will be mainly to describe the basic principles upon which a SEM functions, give its main figures of merit, provide some sample high resolution experimental images, and highlight some promising avenues for future development.

The development of the SEM instrument took place approximately between the years 1925–65, shortly after which the first commercial SEM was launched (McMullan, 1995), and since then, the instrument has undergone many technological improvements (Khursheed, 2011; Goldstein et al., 2017; Brodusch et al., 2018). In particular, over the last few decades, the technique of low voltage scanning electron microscopy (LVSEM) has overcome many traditional limitations. The LVSEM technique has been able to reduce the energy with which the primary electron beam strikes the specimen while at the same time keeping its probe size small by taking advantage of various electron optical innovations, and thereby greatly improving its overall image resolution capability. LVSEMs also have higher signal yields, a smaller beam/specimen interaction volume, greater surface information, and are able to minimize charging effects while inspecting non-conductive specimens. This chapter will describe the SEM instrument mainly in terms of its transformation into the LVSEM.

SEM basic principles

The SEM functions by raster scanning a focused beam of electrons over the surface of a bulk specimen, as shown in Fig. 1a. The beam of electrons, usually referred to as the primary beam, is generated and accelerated to energies from 0.5 to 30 keV inside an electron source unit located at the top of the SEM. The electron source is rotationally symmetric and is designed to emit a round shaped primary beam. The primary beam is emitted with an effective source diameter, energy spread and brightness, and is then subsequently demagnified and focused by a series of electron optical lenses in order to produce a primary electron beam probe of nano-size dimensions that is scanned over the specimen surface.

[☆]*Change History:* November 2022. A Khursheed updated this chapter.

 https://doi.org/10.1016/B978-0-323-90800-9.00128-1

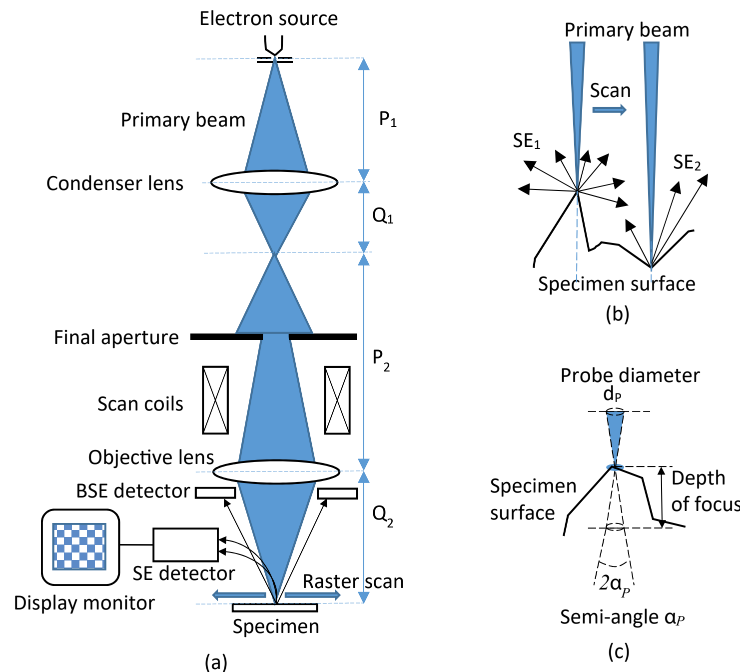

Fig. 1 Schematic drawing of how a scanning electron microscope (SEM) functions. (a) Electron optics of the primary electron beam column. (b) Emission of secondary electrons (SEs) from the specimen surface. (c) Primary beam probe depth of focus.

The number of electron optical lenses required in the column depends on the effective source diameter of the electron source. Fig. 1a depicts two demagnifying lenses, a condenser lens placed just below the electron source, and an objective lens placed just above the specimen. This configuration is widely used for the Schottky electron source (SE), which emits electrons by using the principle of thermal field emission (Bronsgeest, 2014). The amount of demagnification applied to the primary electron beam, M_B, can be estimated by using simple first-order optics principles using the focal spot distances P_1, Q_1, P_2, and Q_2 shown in Fig. 1a. The demagnification factor M_B is given by $(Q_1/P_1).(Q_2/P_2)$. It can also be obtained in terms of the initial source semi-angle α_S ratio with the final beam probe semi-angle α_P, by α_S/α_P. The source spot size needs to be demagnified by a factor of only 5–15 for the Schottky electron source, but for conventional heated tungsten wire electron sources (TE), demagnification factors can range up to 10,000 (Oatley, 1975).

A final circular aperture filters out wide-angle electrons in the primary beam before it enters the objective lens, and a scan unit, usually consisting of magnetic coils, performs the deflection action of raster scanning the primary beam over the specimen surface. The purpose of filtering out wide-angle electrons in the primary beam is to reduce objective lens aberration effects, ensuring that the primary beam electrons striking the specimen have low semi-angles (down to a few millirad) and that they travel close to the objective lens rotational axis of symmetry (within tens of microns). The rotational axis of symmetry of all electron lenses in the SEM is often simply referred to as the SEM's optical axis.

On striking the specimen, the primary beam generates scattered electrons that leave the specimen surface over a wide range of angles and energies. The low energy scattered electrons, known as the secondary electrons (SEs), are attracted on to an electron detector located away to one side of the axis, below the objective lens. The SE energy range is usually defined from 0 to 50 eV, where the upper limit is an arbitrary number having no physical importance. The number of SEs captured by the SE detector is strongly modulated by the specimen's surface topography, as shown in Fig. 1b, which is then translated into image brightness variations on a display monitor. The SE detector signal is amplified and synchronized to the scan deflector unit, so that each scanned point on the specimen corresponds to a single point in the SE display image.

The size of the primary beam focused on to the specimen surface, the probe diameter, d_P, depends not only on the overall demagnification of beam, M_B, but also on the objective lens aberrations. The probe diameter d_P is an important parameter limiting the final SE image resolution, and together with the final semi-angle α_P, it also determines the image depth-of-focus, the specimen depth over which points in the SEM image still appear to be in focus, as illustrated in the schematic diagram shown in Fig. 1c. SEM images have the desirable feature of having a relatively large depth of focus compared to optical microscopes, an advantage which comes from them having relatively small final semi-angles (in the several milli-rad range).

After the primary beam strikes the specimen surface, it loses energy by undergoing a series of multiple collisions inside the specimen, which are largely confined to a balloon shaped region known as the interaction volume, as shown in Fig. 2a. The complex set of events that take place inside the interaction volume generate a cascade of electrons and photons, some of which are able to leave the specimen surface. The lower energy scattered electrons that escape from the specimen surface, the SEs, typically come from

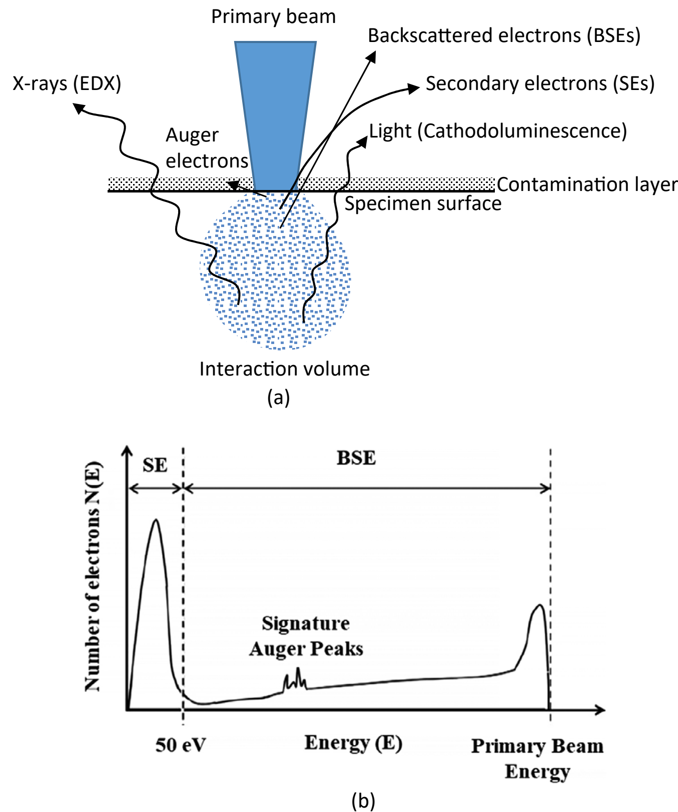

Fig. 2 Electron primary beam-specimen scattering characteristics. (a) Interaction volume and the electron/photons leaving the specimen surface. (b) Energy distribution of the scattered electrons leaving the specimen surface.

nanometer size depths, while the higher energy scattered electrons, the backscattered electrons (BSEs), are typically generated from depths that range from tens to hundreds of nanometers. Since the number of emitted BSEs rises with specimen atomic number, a BSE detector is commonly placed under the objective lens in order to obtain a material contrast image. The BSE image is only capable of providing a map of qualitative material/density changes, and its image resolution is in general significantly poorer than the one provided by the SE image. For these reasons, the BSE image is usually used together with the SE image in order to provide extra material information about the specimen.

Although Auger electrons are generated from even shallower depths inside the specimen than the SEs, they are generally masked by the presence of a nanometer thick hydrocarbon contamination layer. This contamination layer comes from the interaction of the primary beam with the specimen surface and residual gas molecules inside the high vacuum (HV) specimen chamber (10^{-6}–10^{-5} Torr). In practice, the only detectable Auger electrons inside a SEM specimen chamber are those that are generated from within the contamination layer (carbon peak). At micron depths below the specimen surface, characteristic X-rays created from atomic transitions are emitted, and they are used by the energy dispersive X-ray (EDX) spectroscopy technique to perform quantitative material analysis, most commonly used to identify the different types of materials present in the sample. At even lower depths, photons emitted in the 200–800 nm wavelength range are used by the Cathodoluminescence technique in order to provide information about trace elements contained in mineral samples or capture the presence of mechanically induced defects in crystals.

The scattered electrons emitted from the specimen surface have a wide range of energies, as shown in Fig. 2b. The lower part of the distribution is dominated by the SE energy distribution, whose peak typically lies in the 1–2 eV range. In the higher part of the scattered electron energy distribution, there is the BSE peak. Elastically scattered BSEs, known as low loss BSEs, make up the upper part of the electron energy spectrum close to the primary beam energy. Since low loss BSEs emanate from nanometer size depths inside the specimen, they can be used to provide a way of improving the BSE image resolution (Luo and Khursheed, 2007). Detection of low loss BSEs in some SEM columns is achieved by placing high pass energy filters placed in front of the BSE detector.

It is important to note that the SEM does not function like a conventional optical microscope, where a transparent specimen is illuminated by a collimated light beam, and where the subsequent transmitted/scattered light propagating along an optical axis is then magnified into an image by a series of projection lenses. The TEM functions in this way, but not the SEM. Instead of projecting and magnifying a transmitted electron beam into an image, the SEM demagnifies an electron beam coming from an electron source into a nanosize probe which is raster scanned over the surface of the specimen, and its final image is formed from reflected/scattered electrons that leave the specimen. Unlike the parallel action of a TEM, where points from a region of the specimen are

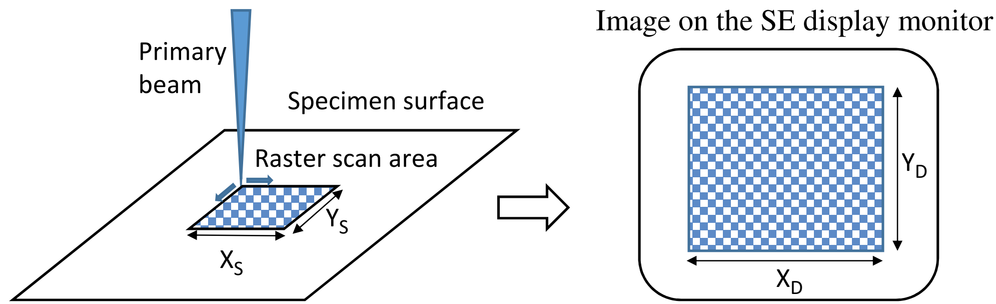

Fig. 3 Schematic drawing of raster scan area on the specimen and its corresponding image on the SE signal monitor display.

simultaneously projected and focused into a set of corresponding points in a final image, an SEM image is formed one point at a time, in a sequential way, similar to how the early generation of cathode ray tubes formed their images, or how an image is formed on a radar screen. In fact, historically, both cathode ray tubes and the invention of radar greatly influenced the way the SEM was invented and subsequently developed (Smith, 1997).

Fig. 3 shows the area of scan on the specimen's surface created by electronic deflection of the primary beam and its corresponding image displayed on the SE monitor. The field of view is given by the area scanned on the specimen surface, (X_S, Y_S), while the image magnification M_I is given by the ratio of the image size displayed on the SE monitor, (X_D, Y_D), to the scan area size on the specimen, X_D/X_S or Y_D/Y_S. It is important not to confuse the electronic image magnification M_I, with the primary beam spot demagnification factor, M_B. The magnification displayed on the monitor screen refers to the electronic image magnification M_I, while the primary beam demagnification factor is not usually given explicitly. A relative indication of its value can be inferred by a "spot size parameter" on the condenser lens settings.

The best achievable image resolution of an SEM is limited by a variety of different factors. Apart from electron optical demagnification/focusing considerations, there are also primary beam-specimen interaction effects. An illustration of how primary beam-specimen interaction effects can limit the spatial resolution of an SEM is shown in Fig. 4, which depicts Monte Carlo simulation results of a primary beam scattering inside a silicon specimen at different primary beam landing energies. The scattering region, approximately equivalent to the interaction volume, effectively generates areas of SE/BSE emission on the surface of the specimen. The size of these emission areas can easily exceed the focused primary beam probe size, and therefore limit SEM image

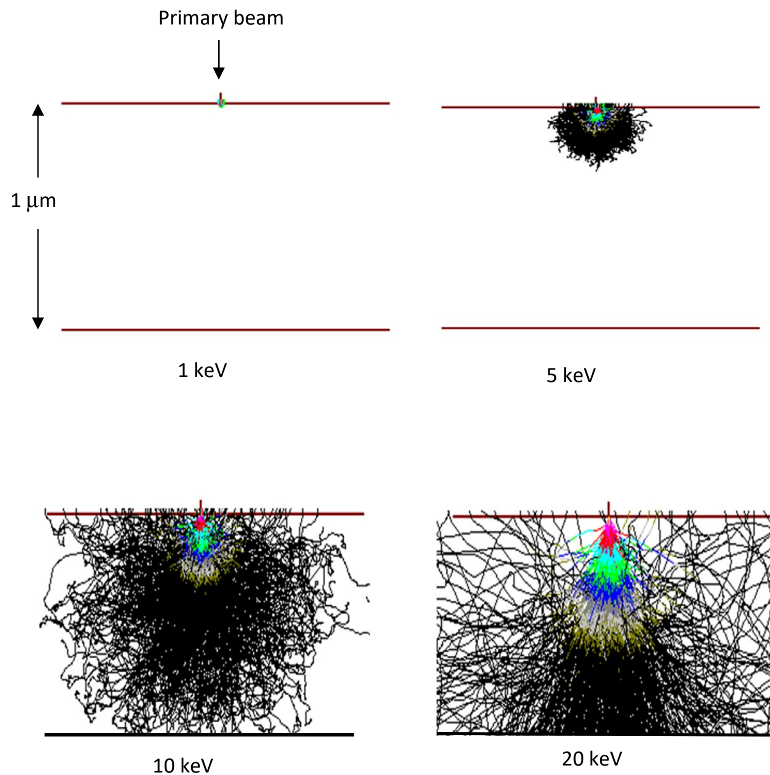

Fig. 4 Monte Carlo simulation of primary electrons striking a silicon sample at energies 1, 5, 10, and 20 keV.

resolution. The Monte Carlo simulations shown in Fig. 4 predict that at a landing energy of 1 keV, the interaction volume is tens of nanometers wide. At 5 keV, the interaction volume is predicted to span hundreds of nanometers. Beyond 10 keV, the simulated interaction volume reaches micron dimensions. Historically, due to poor electron optical performance at low primary beam voltages (<5 kV), the first generation of SEMs were usually operated with primary beam energies in the 5–30 keV range. The simulations shown in Fig. 4 help explain why the first generation of SEMs could only achieve image resolutions in the submicron to micron range.

As already mentioned, significant improvements to SEM image resolution were made when it became possible to lower the landing energy of the primary beam to landing energies of 1 keV or lower, without significantly enlarging the primary beam probe size. Most modern SEMs today function in this way, in the low voltage SEM mode of operation (LVSEM). LVSEM relies on technological advances made in the production of electron detectors, and improvements made in the design of electron sources and objective lenses.

Another advantage of LVSEMs is that they can minimize primary beam induced charging effects while observing non-conductive specimens. The first generation of SEMs needed to sputter non-conductive specimens with a nanometer thick layer of gold or carbon in order to suppress the charging effect. Other advantages of LVSEM over conventional SEMs include them having higher signal yields and that they provide a greater amount of surface information. It is now possible for SEMs to operate with nanometer image resolution on a wide variety of different specimens. LVSEMs are finding an increasing number of applications in subjects such as biology and chemistry which involve observing organic samples directly.

When inspecting a specimen by an SEM, it is important to strike the right balance between acquiring adequate signal-to-noise and minimizing the effects of surface contamination. The main source of noise in the output image comes from shot noise in the primary beam, which for a sufficiently large number of detected electrons has an approximate normal distribution. In most modern SEMs, tens of pA primary beam current in tens of seconds image acquisition time can in principle provide adequate signal-to-noise ratios, but in practice, whether the final captured image is acceptable or not depends on the rate at which the specimen surface carbon contamination layer builds-up.

Contamination on the surface of a specimen is most severe when acquiring high resolution images. This is because high resolution imaging requires small fields of view, which for the same primary beam current and scan rate, leads to larger current densities being present at the specimen surface, and this creates conditions for a greater rate of contamination build-up. The compensating action of adjusting down the primary beam current or total acquisition time when capturing high resolution images partially helps avert this problem, but it can only be done within the constraints of obtaining an adequate output signal-to-noise ratio. For this reason, beam induced contamination is one of the main parameters that limit the ultimate image resolution of SEMs.

The other main beam-specimen interaction parameter limiting image resolution is the interaction volume. Although the interaction volume is made much smaller by operating in LVSEM mode, its finite size also plays an important role in limiting how good the image resolution in an SEM can be. The image resolution limiting role played both by beam induced contamination and the interaction volume helps explain why the same type of electron optical aberration correctors that have worked well for transmission electron microscopes (STEM/TEM) have not worked well for the SEM. Transmission electron microscopes form their output images from a primary electron beam that travels through a thin specimen, in which beam-specimen interaction effects played a relatively minor role compared to electron optical aberrations. In the SEM however, since the image is formed from reflected/scattered electrons that leave the surface of a bulk specimen, beam-specimen interaction effects are much larger, and are comparable in size or greater than the primary beam probe size. Although electron optical aberration correction techniques in the SEM can in principle reduce the primary beam probe to have sub-nanometer diameters, in practice, beam-specimen interactions cause the image resolution limit to be well over a nanometer. There are also inaccuracies caused by mechanical vibrations and electromagnetic interference. At a landing energy of 100 eV, the image resolution of an aberration corrected SEM was found experimentally to be around 2 nm on a test sample having gold particles on a carbon substrate, despite its probe diameter being predicted to be less than 1 nm (Cheng et al., 2019).

On non-conductive samples, there is also the local charging effect. Although LVSEMs are able to achieve an overall global charge balance on a variety of different non-conductive specimens, local charging inevitably occurs over nanometer distances on the specimen surface, and it can distort and deflect the primary beam probe, which in turn can degrade the overall achievable image resolution. This effect causes well known image distortions and resolution limitations in the context of using Critical Dimension (CD) SEM measurements on semiconductor specimens (Arat et al., 2019).

Electron optical figures of merit

The performance of an SEM is critically dependent on the type of electron source being used. The column optics is adjusted so that the projected size of the source on the specimen is small. The energy spread of electrons emitted from the electron source limits the resolution of the SEM at low voltages, and the final image quality depends upon how much current the gun can provide. There have been two types of thermionic sources, and two types of field emission sources used in commercially available SEMs so far.

In the category of thermionic electron sources, there is the tungsten hairpin wire source and the lanthanum hexaboride crystal (LaB_6) source. Both these electron sources form a real crossover point between the cathode and anode. They do this by employing an extra electrode placed between the cathode and anode and biasing it more negatively than the cathode. A current is passed through the cathode and heats it to high temperatures so that electrons are emitted from the cathode surface. The electric field strength at the

cathode surface is relatively low, and a negative space-charge cloud region consisting of slower moving emitted electrons forms in front of the cathode. The emission current settles to an equilibrium value limited by the formation of the space-charge cloud.

Field emission sources function by applying a high electric field between an anode electrode and a finely pointed cathode. The radius of curvature of the cathode tip can be as low as 100 nm and the electric field strength can be several V/nm. Electrons leave the cathode tip via quantum tunneling and do not form a real crossover, instead, they form a "virtual source," which is found by projecting back the emitted rays from the anode plane. The virtual source position typically lies several nanometers behind the cathode electrode tip and ranges from a few to tens of nanometers in diameter. The Schottky electron source supplements its quantum tunneling action with some degree of cathode heating. Cold field emission (CFE) cathodes function at room temperature.

The brightness of an electron gun, β, is an important parameter that characterizes how much current it can provide. The brightness β is defined by

$$\beta = \frac{J}{\pi\alpha^2} \tag{1}$$

where J is the current density and α is the beam semi-angle at the cathode. For a given SEM column, the brightness has a constant value along the primary beam path. The current density at the cathode usually falls off sharply with increasing α. Since the brightness of a gun rises approximately linearly with the anode voltage (primary beam voltage V_p), it is sometimes quoted as the "reduced brightness," β_R, where $\beta_R = \beta/V_p$.

The conservation of brightness along the optical axis provides a means for estimating the primary beam probe current at the specimen surface. If at the specimen, there is a projected source diameter of d_0 and semi-angle of α_0, the primary beam probe current, I_p, is given by

$$I_P = \frac{\pi^2}{4}\beta d_0^2\alpha_0^2 \tag{2}$$

The available probe current is directly proportional to the gun brightness. From this expression, it is clear that high probe currents cannot be obtained with small probe diameters (required for high resolution) and that a compromise between the two must be found. A minimum requirement on the probe current comes from inherent signal-to-noise limitations in the SEM detection/display system.

Each SEM electron source type varies in accordance with the amount of current it can produce, its effective projected size, its intrinsic energy spread, the stability of its emitted current, and its lifetime. Table 1 presents some typical values of these parameters. It should be noted that the values in Table 1 are only approximate, and that some of them depend on the primary beam voltage, such as brightness.

Although the traditional thermionic tungsten hairpin source has the lowest brightness and highest energy spread of all SEM electron sources types, it is reliable, relatively inexpensive, and well understood. For many SEM applications where high brightness and high spatial resolution is not required, and where stable high currents are needed, the thermionic tungsten filament may be used without loss of performance, and may, in fact, be the best choice. The LaB_6 source offers better performance than the tungsten hairpin filament, but it comes at the price of needing to provide a better vacuum level and is more complicated to install and maintain. In practice, the tungsten hairpin filament is much more widely used.

In the category of field emission electron sources, the tungsten cold field emission source has the highest brightness and lowest energy spread, but it faces many difficult technical challenges and is the least reliable of all electron sources for the SEM. It typically requires extreme UHV (XUHV) conditions in order to operate, and its cathode needs to be regularly joule-heated (flashed) every few hours in order to restore degradation of emission caused by the steady build-up of carbon contamination on the cathode tip surface. It also has the highest current instability of all SEM electron source types. For these reasons, although the Schottky electron source is worse from an electron optical performance point of view than tungsten cold field emission sources, it is the most widely used type of field emission source in SEMs.

Fig. 5 shows the kind of magnetic objective lens design that has been widely used in conventional SEM columns. The magnetic objective lens axis is rotationally symmetric, and its axis of symmetry defines the central optical axis for the primary electron beam. A current carrying coil energizes a magnetic circuit made of soft magnetic material, typically an alloy of iron, and a magnetic gap in the circuit creates the axial magnetic field region that focuses the primary electron beam on to the specimen. Fig. 5 shows the simulated flux lines of the Cambridge S100 objective lens design for a coil excitation of 1000 AT and its associated axial field distribution. The

Table 1 Electron source performance comparison.

Source	*Brightness (A/cm^2 sr)*	*Lifetime (hours)*	*Source size*	*Energy spread ΔE (eV)*	*Current stability*	*Vacuum pressure (Pa)*
Tungsten hairpin thermionic source	2×10^4 to 2×10^5	40–100	20–50 μm	1–3	1%	$<10^{-3}$
LaB_6 thermionic source	10^6	200–1000	5–20 μm	0.5–2	1%	$<10^{-5}$
Schottky field emission source	10^7–10^8	>1000	15–30 nm	0.5	2%	$<10^{-7}$
Tungsten Cold field emission source	10^8–10^9	>1000	< 5 nm	0.2–0.3	5%	$<10^{-8}$

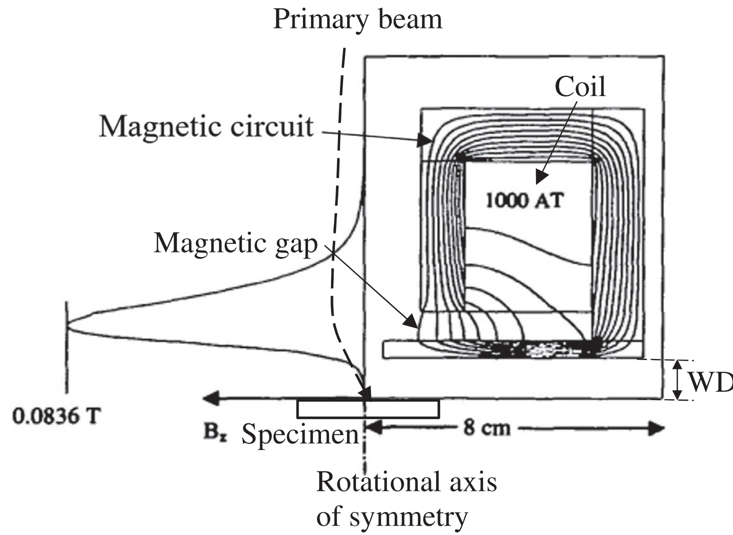

Fig. 5 Simulated on-axis magnetic field distribution $B_Z(z)$ and flux distribution of a conventional Cambridge S100 SEM magnetic objective lens design.

axial field peak field strength is 0.0836 Tesla, capable of focusing a 20 keV primary beam to a point 5 mm below the lower lens pole-piece. The focusing action, illustrated schematically in Fig. 5, comes from the radial variation in objective lens magnetic field intensity. The magnetic field intensity is a minimum on the axis, and it increases in strength radially out toward the pole-pieces. This field distribution causes electrons in the primary beam to rotate about the axis and exerts a radial force on them, pushing them toward the axis. The strength of the radial force increases with off-axis distance, applying a stronger force on the wider angle electrons and a weaker force on the near axis electrons.

The Cambridge S100 objective lens shown in Fig. 5 is an example of a "below-the-lens" design. The specimen in these types of objective lenses is placed in a field free region under the lens assembly. The distance from the specimen to the lens lower pole-piece is known as the working distance (WD), and is similar to the working distance between specimen and objective lens in conventional optical microscopes. Just as in optical microscopes, short focal lengths are required when operating in high magnification mode, which in turn, necessitates the use of short working distances. In practice, SEM columns that use below-the-lens objective lens designs achieve their highest image resolution by setting the working distance to its minimum possible value. Most conventional SEMs have an operational working distance range of around 3–30 mm.

Fig. 6 shows the kind of column lens design used in conventional tungsten hairpin filament SEMs. It consists of two magnetic condenser lenses and a magnetic objective lens. This is different to the Schottky electron source single condenser lens column design shown in Fig. 1a. An extra condenser lens in the case of the conventional tungsten hairpin filament SEM column is required, since the beam crossover size formed inside tungsten hairpin filaments is typically a thousand times bigger than Schottky electron source virtual source sizes.

In addition to limitations in electron optical performance that come from the electron source, objective lens aberrations also play a critical role. In order to keep the aberrations of the objective lens down to an acceptable level, a final aperture is used to filter out the wider angle electrons in the primary electron beam. The final aperture is usually positioned just above the objective lens, and its diameter is selected to keep the semi-angles of electrons reaching the specimen to be typically less than 5 mrad. Fig. 7 shows the kind of lens aberration effects that enlarge the primary beam probe size. They are similar to the kind of aberration effects that exist in optical microscopes.

Spherical aberration is caused by the objective lens over-focusing the wider angle electrons in the primary beam, as shown in Fig. 7a. They travel further off-axis than the narrower angle ones and experience a stronger focusing action acting on them, producing a spherical aberration spot radius r_{SP} which is proportional to the cube of the final semi-angle as follows,

$$r_{SP} = C_S(\alpha_P)^3 \quad (3)$$

where the constant C_S is defined to be the spherical aberration coefficient.

Chromatic aberration comes from the inherent energy spread of electrons in the primary beam. Higher energy primary beam electrons focus at focal points further down the axis than the lower energy primary beam electrons, as shown in Fig. 7b. The change in focal point position along the axis, Δz, varies linearly with relative energy spread, $\Delta E/E$, as follows,

$$\Delta z = C_C(\Delta E/E) \quad (4)$$

where the constant C_C is the chromatic aberration coefficient. In field free focusing regions, the chromatic aberration spot radius, r_{chr}, is given in terms of the final semi-angle α_P by, $r_{chr} = \Delta z\ \alpha_P$.

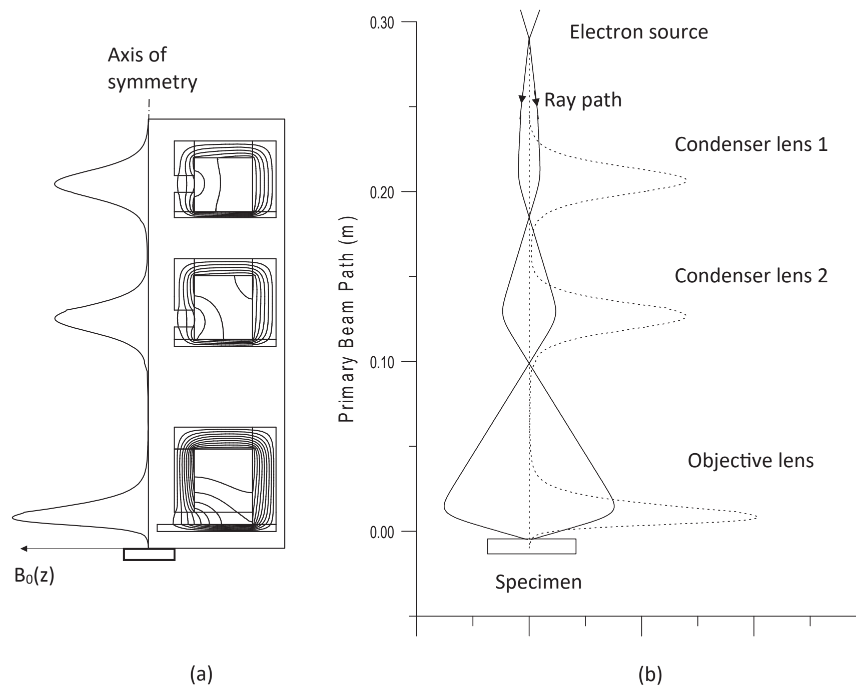

Fig. 6 Simulated ray tracing of the primary electron beam through a column having two magnetic condenser lenses and a S100 objective lens. (a) Axial field distribution. (b) Ray tracing of the primary beam, where the radial coordinate is exaggerated for reasons of scale.

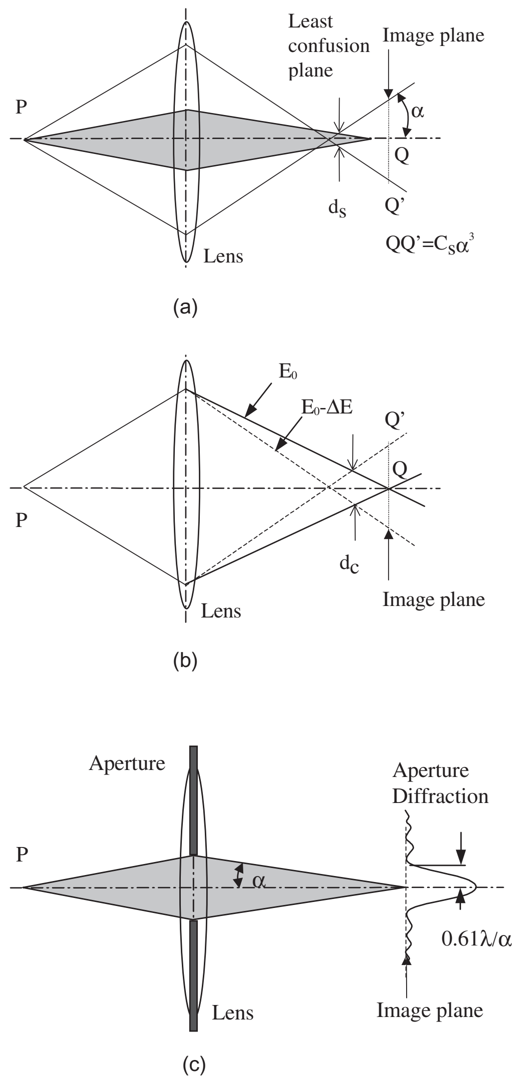

Fig. 7 Schematic drawing illustrating primary electron beam on-axis focusing aberrations. (a) Spherical. (b) Chromatic. (c) Diffraction.

An aperture diffraction aberration spot is also produced at the plane of the specimen. This diffraction effect comes from the intrinsic wave nature of the electrons in the primary beam. As in light optics, the diameter of the diffraction aberration spot produced by a round aperture is 0.61 λ/α_P, where λ is the De Broglie wavelength and α_P is the final semi-angle. The diffraction spot size is taken from the first zero point of a zero order Bessel function radial diffraction distribution, as shown in Fig. 7c. The De Broglie wavelength of an electron beam in an SEM is related to the primary beam voltage V_P by, $\lambda = 1.226/\sqrt{V_P}$, where the primary beam voltage is measured in volts and the wavelength is measured in nanometers. Using this formula, the wavelengths for a beam of electrons at 1 and 25 keV are 38.7 pm and 7.74 pm respectively. Although this wavelength is several orders of magnitude smaller than it is for say a visible light beam, the relatively small final semi-angles used in an SEM, in the mrad range, increases the diffraction spot diameter of the primary beam probe to nanometer sizes, making it comparable in size to the spot diameters produced by spherical and chromatic aberration.

A convenient way of estimating the spatial resolution of a SEM column design is to use the Barth-Kruit root-power-sum formula (Barth and Kruit, 1996), which approximates it to be equivalent to the final probe diameter containing 50% of the primary beam current. This formula has been found to agree well with the more exact wave optical approach, and is widely used to calculate the spatial resolution of an electron objective lens. It uses the electron source parameters of energy spread ΔE, source brightness β, objective lens on-axis spherical aberration coefficient C_S, chromatic aberration coefficient C_C, primary beam current I, landing energy E, beam wavelength λ, and beam final semi-angle α_P. The Barth-Kruit root-power-sum formula for the probe diameter d_P is given by,

$$d_p^2 = \left[\left(d_{sp}^2 + d_{df}^2\right)^{\frac{1.3}{4}} + d_G^{1.3}\right]^{\frac{2}{1.3}} + d_{chr}^2 \tag{5}$$

where, $d_{sp} = \left(\frac{1}{2}\right)^{5/2} C_s \alpha_p^3$

$$d_G = \left(\frac{2}{\pi}\right)\left(\frac{I}{\beta}\right)^{1/2}\frac{1}{\alpha_p}$$

$$d_{chr} = 0.34 C_c \frac{\Delta E}{E}\alpha_p$$

$$d_{df} = 0.54\frac{\lambda}{\alpha_p}$$

Aberration coefficients for objective lenses can be found directly from numerical ray tracing methods, or indirectly by a perturbation method that uses the axial field distribution (Khursheed, 1999). For the Cambridge S100 objective lens shown in Fig. 5 operating in LVSEM conditions, where the lens strength is adjusted to focus a 1 keV beam on to a specimen located at a working distance of 5 mm, the focal length, f, and aberration coefficients, C_S and C_C were simulated by numerical ray tracing to be, $f = 15.69$ mm, $C_S = 30.6$ mm, and $C_C = 13.29$ mm (Khursheed, 2011). Fig. 8 uses these optical parameters to plot the corresponding probe diameter/probe current dependence using the Barth-Kruit formula (Eq. 5) for both thermionic tungsten hairpin filament (TE) and Schottky (SE) electron sources. The TE source here is assumed to have a brightness of 2×10^4 Acm^{-2} sr^{-1} and an energy spread of 2 eV, while the SE source is assumed to have a brightness of 10^7 Acm^{-2} sr^{-1} and an energy spread of 0.5 eV. For every probe current value, the final aperture radius is varied in order to obtain the optimal semi-angle which minimizes the probe diameter.

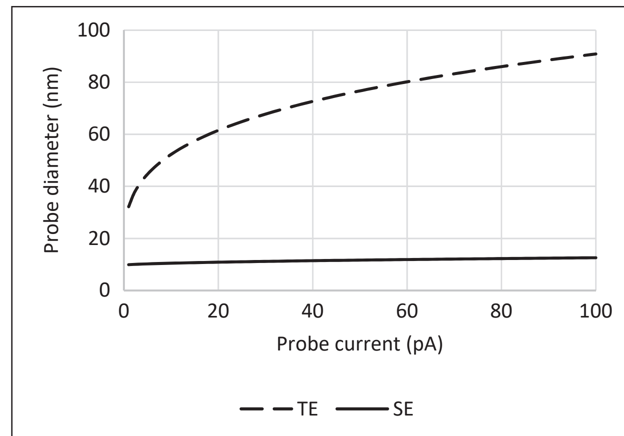

Fig. 8 Simulation of the probe diameter/current dependence of a conventional Cambridge S100 SEM objective lens design using thermionic tungsten hairpin filament (TE) and Schottky (SE) electron sources. The working distance is set to 5 mm for a primary beam energy of 1 keV, and the simulated focusing on-axis aberrations are, $f = 15.69$ mm, $C_S = 30.6$ mm, and $C_C = 13.29$ mm. The TE source is assumed to have a brightness of 2×10^4 Acm^{-2} sr^{-1} and an energy spread of 2 eV, while the SE source is assumed to have a brightness of 10^7 Acm^{-2} sr^{-1} and an energy spread of 0.5 eV.

The simulated probe current-diameter performance shown in Fig. 8 illustrates why the early generation of SEMs, which used a thermionic tungsten hairpin filament combined with a below-the-lens objective lens design, were seldom operated in LVSEM mode. At a primary beam energy of 1 keV, the simulated TE source S100 objective lens simulated probe diameter varies from 50 to 90 nm over the probe current range of 10–100 pA, while the probe diameter of the SE emission source for the same operating conditions stays around 10 nm. The better simulated performance for the SE electron source comes from it having a much higher brightness and lower energy spread than the TE electron source. The image resolution of SEMs that use TE sources is mostly probe current limited when operated in LVSEM mode, while the image resolution of field emission SEMs is generally objective lens aberration limited.

Figs. 9b–d presents schematic diagrams of various LVSEM objective lens design improvements that have been made over the last few decades. Unlike the conventional below-the-lens objective lens layout, shown in Figs. 5 and 9a, they function by either immersing the specimen in a magnetic field, shown in Fig. 9b, or by applying a strong decelerating electric field above the specimen, shown in Fig. 9c, or by combining a decelerating electric field with a magnetic immersion field, shown in Fig. 9d. These objective lens design improvements are known as LVSEM "in-lens" designs since they involve placing the specimen inside objective lens electric/magnetic focusing fields. Another important difference is that since the specimen is now placed inside a lens field distribution, the emitted SEs travel back up through the objective lens bore and are detected either inside the lens assembly or above it (Figs. 9b–d). In conventional objective lens designs, SEs are always detected below the lens assembly (Figs. 5 and 9a).

The LVSEM layout depicted in Fig. 9b uses the magnetic field created around a single conical shaped pole-piece to define a sharply varying field distribution under which the specimen is placed. This kind of lens is sometimes referred to as single-pole lens since its primary beam focusing field is created around only one pole-piece. It is also known as a semi-in-lens design, in order to distinguish it from the kind of full magnetic immersion lens designs used in TEMs, in which the specimen is inserted into a small magnetic gap region between two pole-pieces.

Fig. 10 shows the simulated flux lines of a typical single-pole magnetic semi-in-lens objective lens design. A sharply varying axial magnetic field is projected down into the region immediately below the inner conical pole-piece. The specimen needs to be positioned close to the pole-piece tip with a working distance of only a few millimeters (1–3 mm), so that the primary beam can be

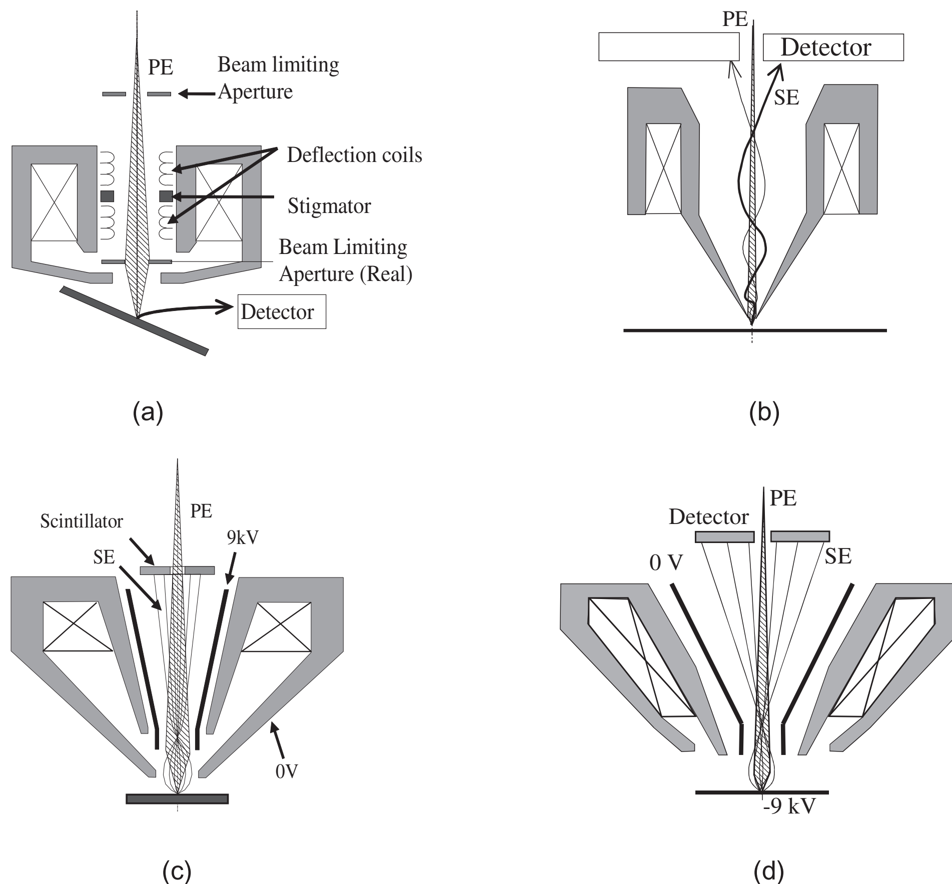

Fig. 9 Different types of objective lens designs used for the SEM. (a) Conventional lens where specimen is placed in a field-free region below the objective lens pole-pieces. (b) Magnetic semi-in lens where the specimen is immersed in a magnetic field region below the lens pole-pieces. (c) Retarding field design using a booster electrode (9 kV) combined with a conventional magnetic objective lens. (d) Retarding field design using negative specimen bias (−9 kV) combined with a magnetic semi-in-lens.

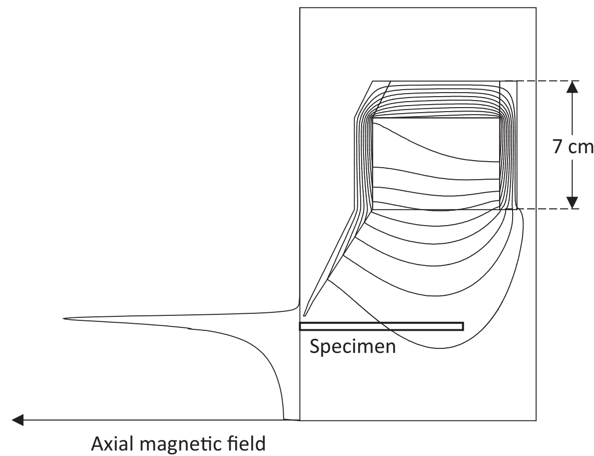

Fig. 10 Simulated flux lines of a single-pole magnetic semi-in-lens objective lens design.

focused on to the specimen with millimeter size focal lengths. This type of objective lens design was reported over three decades ago. For a single pole-piece with an outer slope angle of 45° having an overall pole diameter of 5 mm and a bore diameter of 3 mm, set to focus a 1 keV primary beam on to a specimen located at a working distance of 2.5 mm, its on-axis focusing aberrations were simulated to be $f = 1.8$ mm, $C_S = 1.5$ mm, and $C_C = 1.3$ mm (Shao and Lin, 1989). These lens aberration coefficients are around an order of magnitude smaller than the on-axis aberrations of conventional below-the-lens designs for the same operating conditions.

In the case of the LVSEM design shown in Fig. 9c, a booster electrode (9 kV) keeps the primary beam energy high as it travels down the column (10 keV), and a 0 V specimen retards the beam to have a landing energy of 1 keV. The primary beam is slowed down sharply just before it strikes the specimen, over a distance of only a few millimeters. Since the primary beam travels through most of the magnetic focusing field region at a high energy and is slowed down only in the tail end part of its distribution, the lens on-axis aberrations and focal length are considerably smaller than the case where there is no retarding field. An LVSEM column using the kind of layout shown in Fig. 9c, decelerating a 10 keV primary beam energy down to a landing energy of 1 keV, was reported to have lower on-axis aberrations than corresponding magnetic objective lens designs for LVSEM applications. Frosien et al. for instance, presented a retarding field objective lens design having a C_S less than 3 mm and C_C around 1 mm for a landing energy of 1 keV, in which the specimen was not immersed in a strong magnetic field (Frosien et al., 1995). Unlike most LVSEM columns using magnetic semi-in-lens designs, their objective lens design had the advantage of being able to image magnetic specimens.

From an electron optical point of view, the lowest focusing aberrations are produced by an LVSEM objective lens design that uses a combination of both a magnetic immersion field and a decelerating electric retarding field, such as the lens design shown in Fig. 9d. In this case, a 10 keV primary beam travels down a 0 V column, and is retarded to have a landing energy of 1 keV on a specimen that is biased to −9 kV. This lens design achieves the same strong retarding field electric field action as the retarding field design shown in Fig. 9c, but has the desirable feature of not having to use a booster electrode in the column. At the same time, the specimen is placed in a semi-in-lens magnetic field distribution.

Fig. 11 shows simulated field distributions of a mixed field semi-in-lens LVSEM design based on the one reported by Beck et al. (1995). This lens design uses a 9 kV booster electrode to create a retarding electric field while at the same time is immersing the specimen in a magnetic field. The magnetic field projects down from a large radial gap in the magnetic circuit, as shown in Fig. 11c. Fig. 11b shows the axial electric potential distribution of its decelerating electric field. This type of deceleration action, as well as the semi-in-lens magnetic immersion field distribution, significantly lowers the on-axis aberrations of the objective lens. Beck et al. reported simulated focusing on-axis aberration parameters of $f = 4.24$ mm, $Cs = 0.77$ mm, $Cc = 0.62$ mm for a 10 keV primary beam retarded down to a landing energy of 1 keV at a working distance of 5 mm (Beck et al., 1995).

Fig. 12 presents the probe diameter vs probe current dependence using the Barth-Kruit formula of the three main objective lens designs discussed so far operating with a Schottky electron source at a landing energy of 1 keV. Simulated on-axis aberration parameters are used for the conventional S100 design operating at a working distance of 5 mm, the single-pole magnetic semi-in-lens design operating at a working distance of 2.5 mm, and the mixed field semi-in-lens design operating at a working distance of 5 mm. The results support the general point that the image resolution of FE SEMs for LVSEM applications is mainly aberration limited, and not probe current limited like TE source SEMs (see Fig. 8). The probe diameter for the lens designs shown in Fig. 12 does not change significantly with primary beam current. The probe diameter of the mixed field semi-in-lens design is around a factor of five times smaller than the probe diameter of the conventional S100 objective lens, and about 1 nm smaller than the magnetic semi-in-lens design.

Fig. 13 shows the kind of probe diameter/probe current improvement that can be expected by using a CFE source in combination with semi-in-lens LVSEM designs. The CFE source mixed field semi-in-lens design is predicted to have a probe diameter of around half the probe diameter of a SE source magnetic semi-in-lens column design, a factor of improvement which becomes better with increasing probe current. The predicted probe diameter for the CFE source mixed field semi-in-lens design in the 1–100 pA range lies

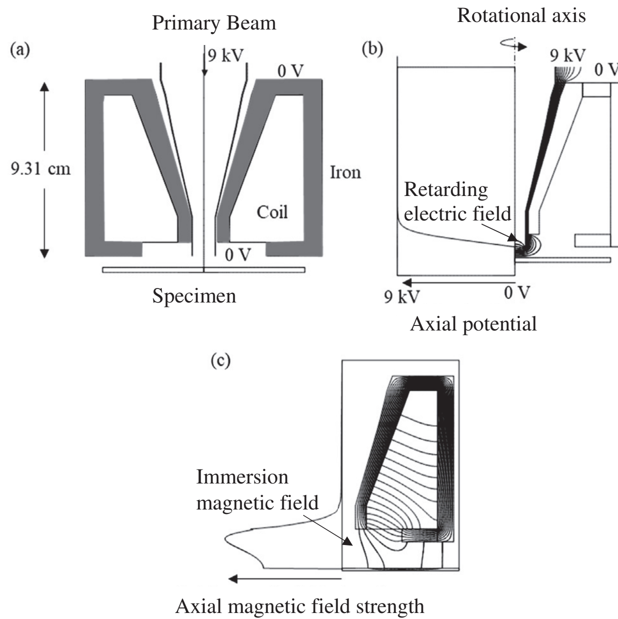

Fig. 11 Simulated field distributions of a LVSEM mixed field semi-in-lens objective lens design based upon the one proposed by Beck et al. (1995). (a) Electrode/excitation coil layout. (b) Retarding electric field distribution. (c) Immersion magnetic field distribution.

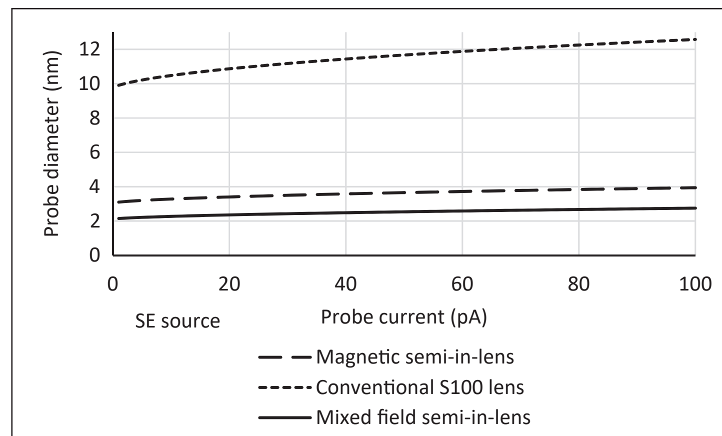

Fig. 12 Simulated probe diameter/probe current dependence for different types of objective lens designs using a SE source operating at a landing energy of 1 keV. The simulated on-axis parameters are, $f = 15.69$ mm, $C_S = 30.6$ mm, and $C_C = 13.29$ mm for a working distance of 5 mm of the S100 lens design, $f = 1.8$ mm, $C_S = 1.5$ mm, and $C_C = 1.3$ mm for a working distance of 2.5 mm of a magnetic semi-in-lens design, and $f = 4.24$ mm, $C_S = 0.77$ mm, and $C_C = 0.62$ mm for a working distance of 5 mm for a mixed field semi-in-lens design. The SE source is assumed to have a brightness of 10^7 $\mathrm{Acm^{-2}\,sr^{-1}}$ and an energy spread of 0.5 eV.

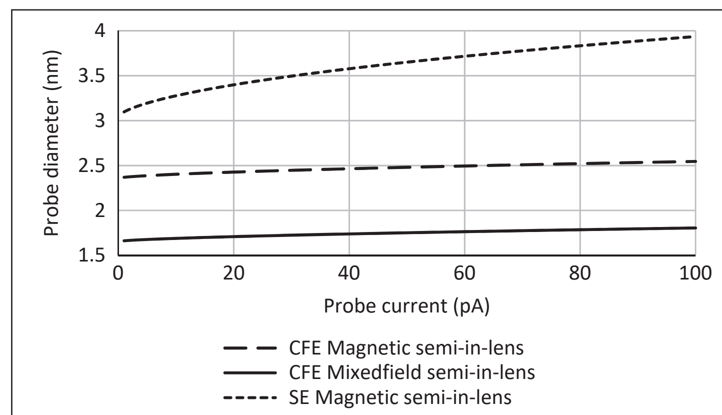

Fig. 13 Simulated probe diameter/current dependence of different LVSEM in-lens designs. The simulated on-axis aberration parameters are $f = 1.8$ mm, $Cs = 1.5$ mm, $Cc = 1.3$ mm for a working distance of 2.5 mm for a magnetic semi-in-lens design, and $f = 4.24$ mm, $Cs = 0.77$ mm, $Cc = 0.62$ mm for a working distance of 5 mm of a mixed field semi-in-lens design. The SE source is assumed to have a brightness of 10^7 $\mathrm{Acm^{-2}\,sr^{-1}}$ and an energy spread of 0.5 eV, and the CFE source is assumed to have a brightness of 10^8 $\mathrm{Acm^{-2}\,sr^{-1}}$ and an energy spread of 0.3 eV.

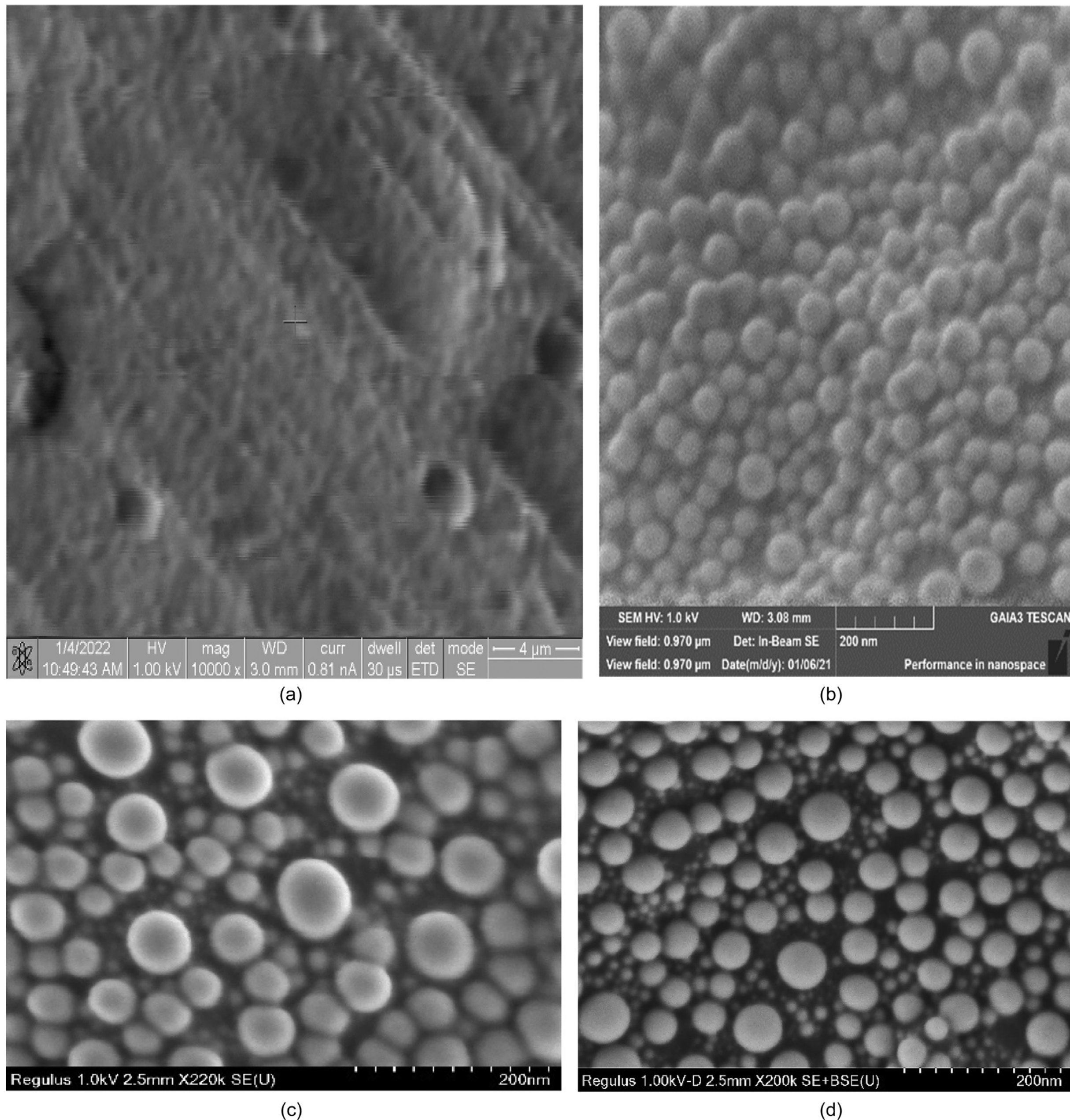

Fig. 14 Comparison of experimental images from different SEM designs taken at a landing energy of 1 keV of a tin balls-on-carbon calibration specimen. The diameter of the tin balls ranges from a few nanometers to around 60 nm. (a) Image from a conventional thermionic tungsten hairpin source below-the-lens SEM design operating at a working distance of 3 mm. The image magnification is 10,000 and was obtained from a dual beam FEI Quanta 200 3D FIB-SEM. (b) Image from a Schottky electron source magnetic semi-in lens SEM operating at a working distance of 3.08 mm. The image was obtained from a Tescan Gaia3 FIB-SEM. (c) Image from a cold field emission electron source magnetic semi-in-lens SEM operating at a working distance of 2.5 mm and image magnification of 220,000. The image was obtained from a Hitachi Regulus 8230 SEM. (d) A cold field emission electron source semi-in-lens SEM operating in retarding field mode with a working distance of 2.5 mm and image magnification of 200,000. A 3 keV primary beam was used with a—2 kV specimen bias. The image was obtained from a Hitachi Regulus 8230 SEM.

well below 2 nm. In practice, LVSEMs rarely achieve an image resolution of better than 2 nm at a landing energy of 1 keV. This limitation comes mainly from environmental disturbances such as mechanical vibrations and electromagnetic interference, as well as beam-specimen interaction effects.

Fig. 14 shows experimental images from different SEM columns, each having a different electron source/objective lens combination. A calibration specimen consisting of tin balls-on-carbon was used, where the diameter of the tin balls ranged from a few nanometers to around 60 nm. Details about each SEM column design and the operating conditions used are given in the figure caption. These experimental images generally confirm the probe diameter/probe current simulation predictions shown in

Figs. 8, 12, and 13. The tin balls are not visible in the image provided by the conventional thermionic tungsten hairpin source shown in Fig. 14a, which uses a below-the-lens objective lens design. In order to focus this image, broader topographical features on the specimen were used. The next best image resolution is provided by the Schottky source magnetic semi-in-lens column design, shown in Fig. 14b. The bigger size tin balls are visible in this image. A further improvement is obtained by the CFE source magnetic semi-in-lens SEM column image shown in Fig. 14c, in which some of the smaller tin balls become visible. However, the best image, shown in Fig. 14d, is obtained by the CFE magnetic semi-in-lens SEM column operating in retarding field mode (mixed field semi-in-lens). Small nano-size tin balls are clearly visible in this image.

Summary and future directions

This chapter has summarized SEM basic principles, presented its main figures of merit, and provided an illustration of its high resolution experimental images. The chapter has highlighted instrument developments mainly in the context of low voltage scanning electron microscopy (LVSEM). Looking ahead, there are several other future promising lines of development.

Aberration corrected SEMs might prove useful for some specialized ultra-low voltage/high current applications, but are unlikely to become new general purpose SEMs. This is because SEM image resolution limitations are mainly set by specimen-beam interaction effects, such as the size of the interaction volume and beam induced contamination. These effects already limit the best achievable LVSEM image resolution to lie somewhere between 1 and 2 nm for most bulk specimens, so further reduction of the projected primary electron beam probe size into the sub-nanometer range is unlikely to provide image resolution improvement.

Further work on making cold field-emission (CFE) sources more reliable and easier to use is another promising line of development. Research is presently being carried out on the possibility of using different CFE cathodes, apart from the conventional tungsten one. However, none of them are as yet in a form that can be reliably used in commercial SEMs. Another area of SEM development receiving attention is the challenge of miniaturizing SEM columns, especially for the purpose of making large multi-column LVSEM arrays that can inspect semiconductor wafer specimens. Multi-beam SEM designs have proven to be feasible, where an array of beamlets are created from a single source. However, they have a relatively small overall field of view, typically in the sub-millimeter range, and the optics of each beamlet cannot be individually tuned. The next stage of development will be to make a LVSEM column array that can provide parallel inspection of a large specimen, where each column has its own separate source with individually tunable electron optics.

Another promising area of SEM development is to explore ways of reducing beam induced contamination. Beam induced contamination effects limit both LVSEM ultimate image resolution and image signal-to-noise. Specimen preparation methods borrowed from UHV electron spectroscopy chambers might prove useful, such as pre-cleaning the specimen by low energy ion bombardment or applying UV irradiation.

Finally, there is the possibility of using electron energy spectroscopy techniques inside the SEM. At present, LVSEM lacks a companion material science tool. This is because EDX only functions well for primary beam landing energies of 6 keV or higher, and the landing energies inside LVSEM systems, of 2 keV or less, are not high enough to generate the necessary atomic transitions that emit characteristic X-rays. In principle, energy spectroscopy of SEs and BSEs has the potential for developing new material analysis tools for LVSEM, acquiring material information in a manner similar to Auger electron spectroscopy (AES) or reflection electron energy loss spectroscopy (REELS). The success of this approach will also most likely depend on how effectively beam induced contamination effects can be reduced.

Acknowledgments

The author would like to acknowledge the help of Dr. Zheng Minrui, a Research Fellow at the National University of Singapore, for carrying out the research work to obtain the SEM experimental images presented in this chapter.

Conflict of Interest

The author declares that there is no conflict of interest.

References

Arat KT, Klimpel T, and Hagen CW (2019) Model improvements to simulate charging in scanning electron microscope. *Journal of Micro/Nanolithography, MEMS and MOEMS* 18(4): 044003.

Barth JE and Kruit P (1996) Addition of different contributions to the charged particle probe size. *Optik* 101(3): 101–109.

Beck S, Plies E, and Schiebel B (1995) Low voltage probe forming columns for electrons. *Nuclear Instruments and Methods in Physics Research A* 363: 31–42.

Brodusch N, Demers H, and Gauvin R (2018) *Field Emission Scanning Electron Microscope, New Perspectives for Materials Characterization*. Springer Publisher.

Bronsgeest M (2014) *Physics of Schottky Electron Sources, Theory and Optimum Operation*. Jenny Stanford Publishing.

Cheng ZH, Dohi H, Hayashi S, Hirose K, and Kazumi H (2019) Application of aberration corrected low voltage SEM for metrology. In: *Proc. SPIE 10959, Metrology, Inspection, and Process Control for Microlithography XXXIII, 1095922*.

Frosien J, Lanio S, and Feuerbaum HP (1995) High precision electron optical system for absolute and CD-measurements on large substrates. *Nuclear Instruments and Methods in Physics Research A* 363: 25–30.

Goldstein JI, Newbury DE, Michael JR, Ritchie NWM, Scott JHJ, and Joy DC (2017) *Scanning Electron Microscopy and X-Ray Microanalysis*. Springer.

Khursheed A (1999) *The Finite Element Method in Charged Particle Optics*. Kluwer Academic Publishers.

Khursheed A (2011) *Scanning Electron Microscope Optics and Spectrometers*. World Scientific Publishers 29.

Luo T and Khursheed A (2007) Imaging with surface sensitive backscattered electrons. *Journal of Vacuum Science and Technology B* 25(6). https://doi.org/10.1116/1.2781523.

McMullan D (1995) Scanning electron microscopy 1928-1965. *Scanning* 17(3): 175–185.

Oatley CW (1975) The tungsten filament gun in the scanning electron microscope. *Journal of Physics E: Scientific Instruments* 8: 1037.

Shao Z and Lin PSD (1989) High resolution low-voltage electron optical system for very large specimens. *Review of Scientific Instruments* 60(11): 3434–3441.

Smith KCA (1997) Charles Oatley: Pioneer of scanning electron microscopy. In: Rodenburg JM (ed.) *Electron Microscopy and Microanalysis*. CRC Press.